ISSN 0021-3640, JETP Letters, 2022, Vol. 115, No. 5, pp. 267–275. © The Author(s), 2022. This article is an open access publication, corrected publication 2022.
ISSN 0021-3640, JETP Letters, 2022. © Pleiades Publishing, Inc., 2022.

CONDENSED MATTER

Josephson Spin-Valve Realization in the Magnetic Nodal-Line Topological Semimetal Fe_3GeTe_2

O. O. Shvetsov[a], Yu. S. Barash[a], A. V. Timonina[a], N. N. Kolesnikov[a], and E. V. Deviatov[a, *]

[a] *Institute of Solid State Physics, Russian Academy of Sciences, Chernogolovka, Moscow region, 142432 Russia*

**e-mail: dev@issp.ac.ru*

Received January 11, 2022; revised January 13, 2022; accepted January 13, 2022

Three-dimensional van der Waals ferromagnet Fe_3GeTe_2 (FGT) is regarded as a candidate for the magnetic topological nodal line semimetal. We investigate lateral electron transport between two 3 μm spaced superconducting In leads beneath a thick three-dimensional FGT exfoliated flake. At a low temperature of 30 mK, we observe Josephson supercurrent that exhibits unusual critical current I_c suppression by the magnetic field B. The overall $I_c(B)$ pattern is asymmetric in respect of the sign of the magnetic field B. We demonstrate, that the asymmetry is defined by the magnetic field sweep direction, so the $I_c(B)$ pattern is strictly reversed (as magnetic field reversal) for the opposite sweeps. We also observe an interplay between maximum and minimum in $I_c(B)$ in normal magnetic fields, while there are fast aperiodic $I_c(B)$ fluctuations for the in-plane ones. These effects cannot be expected for homogeneous superconductor-ferromagnet-superconductor junctions, while they are known for Josephson spin valves. The mostly possible scenario for Josephson spin valve realization in FGT is the misalignment of spin polarizations of the Fermi arc surface states and ferromagnetic FGT bulk, but we also discuss possible influence of spin-dependent transport between magnetic domains.

DOI: 10.1134/S0021364022100101

1. INTRODUCTION

Recently, Fe_3GeTe_2 (FGT) has attracted significant attention as a promising platform for novel physical phenomena, which are connected with magnetic and electronic non-trivial topology. FGT is an itinerant van der Waals ferromagnet characterized by an out-of-plane magnetocrystalline anisotropy both for three-dimensional single crystals and down to two-dimensional limit, which was confirmed by theoretical and experimental investigations [1–6]. Experimentally, FGT shows large anomalous Hall [7, 8] and Nernst [9] effects, topological Hall effect [10] and Kondo lattice physics [11]. From the view of the electronic band structure, three-dimensional FGT is a unique candidate for the ferromagnetic nodal line semimetal [8], hosting spin-polarized Fermi arc surface states [12].

Different realizations of spin valves are known for magnetic materials. Usually, spin valves are realized as ferromagnetic multilayers [13, 14] with different layer thicknesses. The multilayer resistance depends on the mutual orientation of their magnetizations due to the spin-dependent scattering, so the resistance can be affected by external magnetic field or high current density. Due to the different spin polarization of the Fermi arc surface states and ferromagnetic bulk, magnetic topological materials should also demonstrate spin-valve transport properties [15–18]; i.e., they can be regarded as natural realization of spin-valves. In this case, spin-polarized Fermi arcs and ferromagnetic bulk represent thin (free) and thick (reference) layers, respectively.

In proximity with a superconductor, topological surface (or edge) states are able to carry supercurrents over extremely large distances [19–23]. For the magnetic topological materials it naturally implies spin triplet superconductivity, which is the mutual effect of superconductivity, exchange interaction and spin–orbit coupling [24–29]. Triplet supercurrent can be expected, e.g., for a Josephson spin valve [30–34] (JSV), where ferromagnetic multilayer is sandwiched between two superconducting electrodes. In the majority of devices the Josephson current is directed perpendicular to the layers, but the spin-valve effects can also occur in systems, where the supercurrent flows along the planes [35].

In JSVs, supercurrent is defined mainly by the relative orientation of the layers' magnetizations, while in conventional Josephson junctions it is modulated by magnetic flux. For the supercurrent flowing perpendicular to the layers, such a dependence on relative orientations of the layers' magnetizations was studied in detail [30]. Due to the natural spin-valve realiza-

tion, magnetic topological semimetals like FGT may be regarded as a platform for planar JSV investigations.

Symmetry analysis and first principles calculations have shown, that the inversion symmetry breaking can occur at the FGT interface [36]. Noncentrosymmetric interfacial effects are known to be able to substantially influence the charge transport in magnetic systems, in particular via the spin–orbit torque, and to result in unidirectional transport properties [37–41]. In proximity with superconductivity, broken inversion and time reversal symmetry can generally lead to asymmetries of the Josephson current with respect of the magnetic field reversal, e.g., due to chiral properties of the topologically protected states [42, 43]. In superconducting heterostructures with non-coplanar magnetization textures, breaking the magnetization reversal symmetry can result in the direct coupling between the magnetic moment and the supercurrent, and in the anomalous Josephson effect [44–48].

Here, we investigate lateral electron transport between two 3 μm spaced superconducting In leads beneath a thick three-dimensional FGT exfoliated flake. At low 30 mK temperature, we observe Josephson supercurrent that exhibits unusual critical current I_c suppression by the magnetic field B. The overall $I_c(B)$ pattern is asymmetric in respect to the B sign. We demonstrate, that the asymmetry is defined by the magnetic field sweep direction, so the $I_c(B)$ pattern is strictly reversed (as B to $-B$ inversion) for the opposite sweeps. We also observe an interplay between maximum and minimum in $I_c(B)$ in normal magnetic fields, while there are fast aperiodic $I_c(B)$ fluctuations for the in-plane ones. These effects cannot be expected for homogeneous superconductor-ferromagnet-superconductor junctions, while they are known for Josephson spin valves.

2. SAMPLES AND TECHNIQUE

Fe_3GeTe_2 was synthesized from elements in evacuated silica ampule in a two-step process. At the first step, the load was heated up to 470°C at 10°C/h rate and the ampule was held at this temperature for 50 h. At the second step, the temperature was increased up to 970°C with the same rate. After 140 h exposure, the ampule was cooled down to the room temperature at a rate of 5°C/h. X-ray diffraction data indicates, that the iron tellurides FeTe and $FeTe_2$ were also found in the obtained material, in addition to the expected Fe_3GeTe_2 compound.

To obtain Fe_3GeTe_2 single crystals, the synthesized mixture was sealed in evacuated silica ampule with some admixture of iodine. The transport reaction was carried out for 240 h with temperatures 530 and 410°C in hot and cold zones, respectively. Afterward, the ampule was quenched in a liquid nitrogen. Water-solvable iron and tellurium iodides were removed in hot distilled water from the obtained Fe_3GeTe_2 single crystals, so the powder X-ray diffraction analysis confirms single-phase Fe_3GeTe_2 with $P63/mmc$ (194) space group ($a = b = 3.991(1)$ Å, $c = 16.33(3)$ Å) (see Fig. 1a). The known structure model [49] Fe_3GeTe_2 is also refined with single crystal X-ray diffraction measurements (Oxford diffraction Gemini-A, Mo $K\alpha$). The Fe_3GeTe_2 composition is verified by energy-dispersive X-ray spectroscopy.

Non-trivial surface properties are only known for three-dimensional topological semimetal single crystals [50]. Thus, we use thick (1 μm) FGT flakes, which are obtained by a mechanical cleavage from the initial single crystal.

Figure 1b shows a top-view image of a FGT flake with underlying indium leads. The leads pattern is formed by lift-off technique after thermal evaporation of 100 nm In on the insulating SiO_2 substrate. The 10 μm wide leads are separated by 3 μm intervals. One FGT flake is transferred to the substrate with the defined In leads pattern and pressed to the leads slightly. No stress is needed for a flake to hold on the In leads afterward. This procedure allows to create transparent FGT-In interfaces [51–53] without mechanical polishing or chemical treatment, and to protect the relevant (bottom) FGT surface from any oxidation or contamination.

To confirm FGT quality, magnetoresistance measurements are performed also in standard Hall bar geometry for reference samples with normal (Au) leads. In Fig. 1c longitudinal magnetoresistance R_{xx} is monotonic and negative in normal magnetic fields (red curve, right axis), while it shows a kink at 3.5 T for the in-plane configuration (blue curve, left axis). This behavior coincides well with the previously reported results [10]. Another specific feature of time reversal symmetry breaking in topological semimetals is a large anomalous Hall effect, which manifests itself as nonzero Hall conductance in zero magnetic field. The anomalous Hall effect can be regarded as the indication to a magnetic topological phase, as supported by the topological-insulator-multilayer model, where the two-dimensional Chern edge states form the three-dimensional surface states [50]. The anomalous Hall effect is shown in Fig. 1d for normal field orientation, while hysteresis in R_{xy} is also known for the in-plane field as a novel planar Hall effect (see Fig. 1e). The latter has been also recognized as topological Hall effect related to the complicated spin structures in FGT [10].

We study electron transport between two neighbor In leads in a standard four-point technique (see Fig. 1b). All the wire resistances are excluded, which is necessary for low-impedance samples. To obtain $dV/dI(I)$ characteristics, dc current is additionally modulated by a low 2 μA (below the dc current step) ac component at a 1107 Hz frequency. We measure the ac component of the potential drop ($\sim dV/dI$) by lock-in. The signal is confirmed to be independent of the

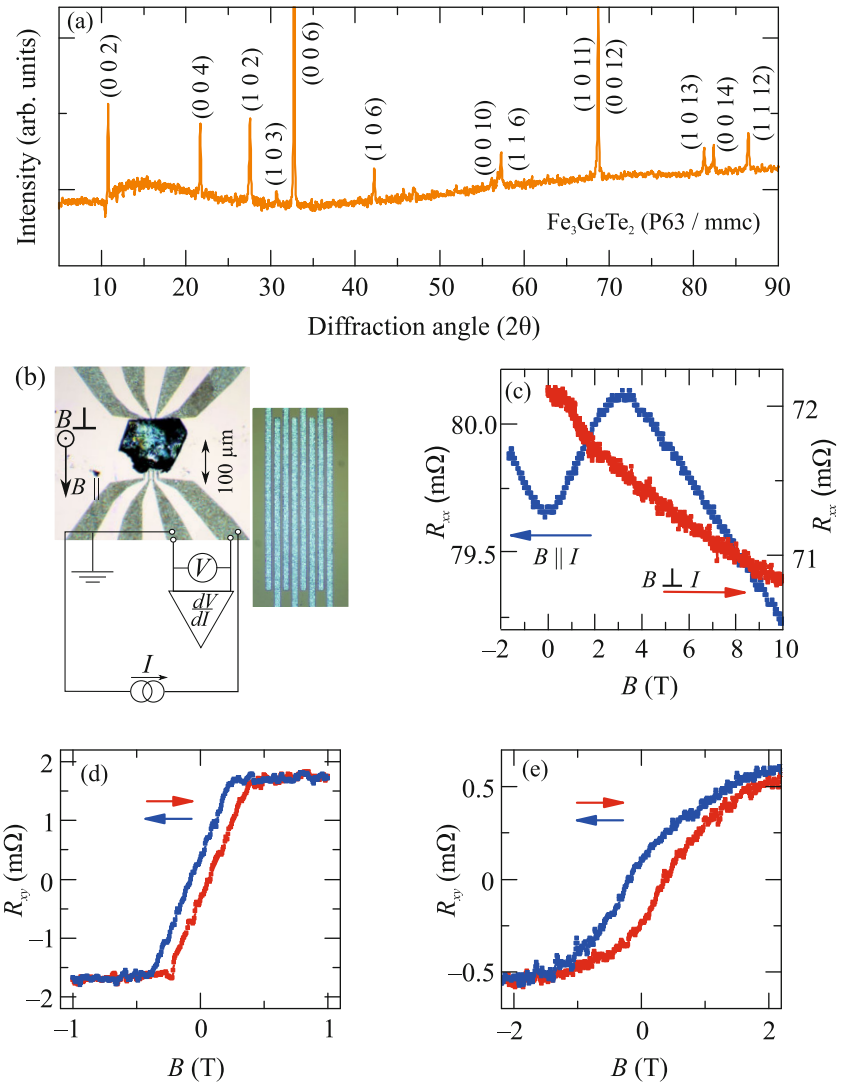

Fig. 1. (Color online) (a) X-ray diffraction pattern (Cu$K\alpha$1 radiation, $\lambda = 1.540598$ Å), which confirms single-phase Fe_3GeTe_2 with $P63/mmc$ (194) space group ($a = b = 3.991(1)$ Å, $c = 16.33(3)$ Å). (b) A top-view image of the sample with electrical connections. A thick (1 μm) single-crystal FGT flake is placed by the flat bottom surface on the pre-defined superconducting In leads. The right inset shows the initial leads pattern, which consists of 10 μm wide indium stripes separated by 3 μm intervals. Electron transport is investigated between two neighbor In leads in a standard four-point technique, all the wire resistances are excluded. Arrows indicate the in-plane $B_\parallel$ and normal $B_\perp$ magnetic field orientations for Figs. 3 and 4. (c–e) Magnetoresistance measurements, to confirm FGT quality, for a reference sample with Au leads in standard Hall bar geometry. (c) Longitudinal magnetoresistance R_{xx} for the in-plane (left axis, blue curve) and for the normal (right axis, red curve) fields. (d, e) Hall $R_{xy}(B)$ hysteresis loops in normal and in-plane fields, respectively, which is usually ascribed to anomalous and topological Hall effects in FGT [10]. The arrows denote magnetic field sweep directions.

modulation frequency within 100 Hz–10 kHz range, which is defined by the applied filters. The measurements are performed within the temperature range of 30 mK–1.2 K.

3. EXPERIMENTAL RESULTS

Figure 2 clearly demonstrates Josephson effect for two different samples, which are referred as S1 and S2. Qualitative behavior is similar, despite strongly different critical current I_c and normal resistance values.

As expected, the zero-resistance state appears below some critical temperature, which is about 0.88 and 0.34 K for the devices in Figs. 2a and 2b. These In-FGT-In junctions are characterized by different maximum supercurrent values $I_c = 0.17$ mA (S1) and 0.018 mA (S2).

The high temperature curves are typical for Andreev reflection in Fig. 2. The superconducting gap positions are defined by symmetric resistive dV/dI features at low currents, they are denoted by dashed

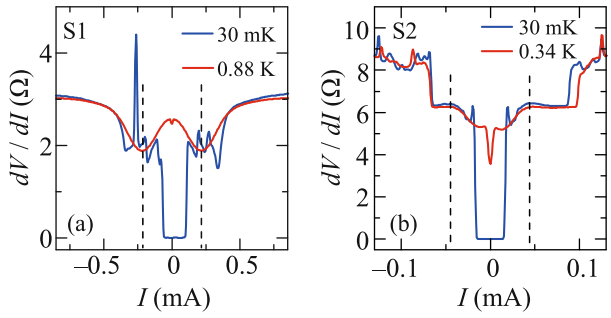

Fig. 2. (Color online) Josephson effect for two different samples with In-FGT-In junctions (S1 and S2 in (a) and (b), respectively). Qualitative behavior is similar, despite strongly different critical current ($I_c = 0.17$ mA in (a) and 0.018 mA in (b)) and normal resistance values. The zero-resistance state appears below 0.88 K for S1 and 0.34 K for S2. The high-temperature curves are typical for Andreev reflection. The superconducting gap positions are denoted by the dashed lines (see the main text), it should not be confused with asymmetric jumps in dV/dI at much higher currents. The data are presented for zero magnetic field.

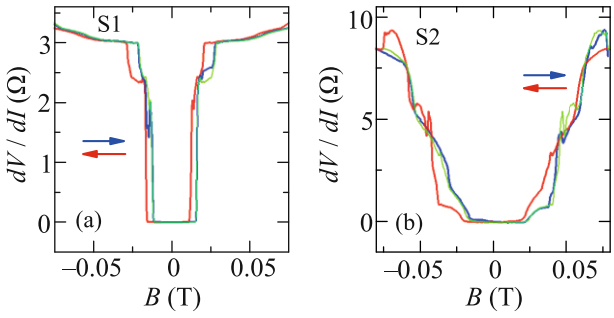

Fig. 3. (Color online) Influence of the external in-plane (a) and normal (b) magnetic fields on Josephson effect at $T = 30$ mK for S1 and S2, respectively. $dV/dI(B)$ curves are not symmetric in respect to zero field, the observed asymmetry depends on the magnetic field sweep direction: red and blue curves are for two opposite sweeps, the sweep direction is denoted by arrows of the corresponding color. All the dV/dI features are mirrored for these curves, so $dV/dI(B)$ curves are strictly reversed for two sweep directions. This curve reversal is demonstrated by nearly perfect coincidence of the blue and green curves, which are obtained as the B to $-B$ inversion of the red ones. The reversal cannot be expected for a superconductor-ferromagnet-superconductor junction with the homogeneous magnetization of the ferromagnetic layer, but it is a fingerprint of the complicated spin structures. The data are obtained at 30 mK.

lines in Fig. 2. For S1, $\Delta_{S1} = 0.42$ meV is obtained from ± 0.22 mA dV/dI feature positions and 1.9 Ω resistance level in Fig. 2a. Δ_{S2} can also be estimated as 0.28 meV in Fig. 2b. These gap values are reasonable for In-FGT-In junctions, since the bulk 0.5 meV In gap should be partially suppressed by the intrinsic FGT magnetization.

Since FGT is an uniaxial ferromagnet, which is confirmed by the Hall curves in Figs. 1d and 1e, it seems to be reasonable to investigate Josephson effect in differently oriented magnetic fields. On the other hand, In-FGT junctions are known to be badly reproduced in different cooling regimes, which restricts the possibilities to remount a sample in the dilution refrigerator. For these reasons, qualitatively similar samples S1 and S2 are initially mounted in the in-plane and normal field orientations, respectively, to avoid unwanted influence of the cooling procedure on the experimental data.

Figure 3 demonstrates the influence of external in-plane (a) and normal (b) magnetic fields on sample resistance at $T = 30$ mK for S1 and S2, respectively. The result is qualitatively similar for both field orientations: the zero-resistance state is suppressed by the external field, $dV/dI(B)$ curves are not symmetric with respect to the zero field value.

As a most important, the observed $dV/dI(B)$ asymmetry depends on the magnetic field sweep direction. Moreover, all the dV/dI features are mirrored for the opposite (blue and rad colors) field sweeps, so $dV/dI(B)$ curves are strictly reversed for the two sweep directions in Figs. 3a and 3b. This curve reversal is demonstrated by nearly perfect coincidence of the blue and green curves in Fig. 3, which are obtained as the B to $-B$ inversion of the red ones. The reversal cannot be expected for a superconductor-ferromagnet-superconductor (SFS) junction with the homogeneous magnetization of the central ferromagnetic layer. In contrast, it is known to be a fingerprint of the complicated spin structures, like ferromagnetic domains or multilayer in Josephson spin valves [30–34]. Figure 3 also excludes any possibility for the unwanted shortings of the In leads, since a simple In-In junction cannot demonstrate the observed $dV/dI(B)$ reversal.

$dV/dI(B)$ reversal can also be demonstrated by colormaps in Figs. 4a, 4b and 4d, 4e for samples S1 and S2, respectively. The colormaps are obtained from $dV/dI(I)$ curves at fixed magnetic field values, which are changed point-by-point in up or down directions. To establish definite sample magnetization state, every magnetic field sweep cycle begins from high field value $B = \pm 100$ mT. Due to the procedure, $dV/dI(B)$ reversal is not connected with any time-dependent relaxation. The panels (a) and (b) differ by the magnetic field sweep directions in Fig. 4, which is from negative to positive values in (a) and is just opposite in (b). The previously described $dV/dI(B)$ reversal can be clearly seen, e.g., by the asymmetric black feature at ±9 mT in Figs. 4a, 4b. The reversal effect is even more pronounced in (d) and (e) for normal magnetic fields.

For Josephson effect, an important information can be obtained from the maximum supercurrent I_c suppression. In principle, zero-resistance black region

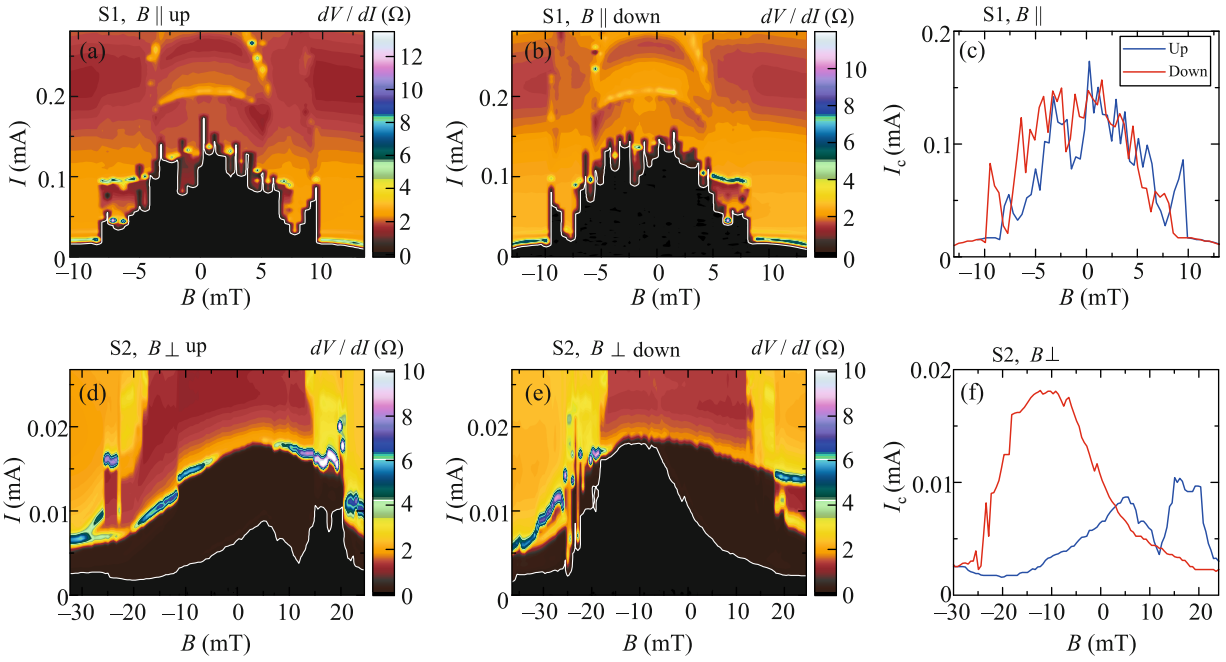

Fig. 4. (Color online) Colormaps of $dV/dI(I, B)$ for samples S1 and S2 in (a, b) and (d, e), respectively. The panels (a, d) and (b, e) differ by the magnetic field sweep direction, which is from negative to positive values in (a) and is just opposite in (b). All the data are obtained at 30 mK. To establish definite sample magnetization, every magnetic field sweep begins from high field value $B = \pm 100$ mT (the sign depends on the sweep direction). The colormaps are obtained from $dV/dI(I)$ curves at fixed magnetic field values, which are changed point-by-point in up or down directions. To establish definite sample magnetization state, every magnetic field sweep cycle begins from high field value $B = \pm 100$ mT. The $dV/dI(B)$ reversal from Fig. 3 can be clearly seen, e.g., by the asymmetric black feature at ± 9 mT in (a, b). The reversal effect is even more pronounced in (d, e) for normal magnetic fields. (c, f) $I_c(B)$ dependencies for the in-plane and normal magnetic field orientations, respectively. The general $I_c(B)$ shapes are asymmetric in both cases, the asymmetry is reversed for the up (blue) and down (red) field sweeps. For the in-plane magnetic fields, $I_c(B)$ shows well-reproducible aperiodic fluctuations in (c). On the contrary, no noticeable fluctuations can be observed in (f). In normal magnetic fields, there is an interplay between maximum and minimum in $I_c(B)$ at ± 12 mT, which is well known for the Josephson spin valves [30–34]. The data are obtained at 30 mK.

in the colormaps reflects the critical current $I_c(B)$ suppression pattern, as it is emphasized by the white envelope curves in Figs. 4a, 4b and 4d, 4e. To obtain I_c with high accuracy at fixed B, we sweep the current ten times from the zero value (i.e., from the superconducting $dV/dI = 0$ state) to some value well above the I_c (the resistive $dV/dI > 0$ state) and then determine I_c as an average value of dV/dI breakdown positions. The result is presented in Figs. 4c and 4f for two magnetic field orientations, respectively. The general $I_c(B)$ shape is asymmetric in both cases, the asymmetry is reversed for the up (blue) and down (red) field sweeps. The critical current $I_c(B)$ also does not exhibit a conventional Fraunhofer pattern [54, 55].

There are also some features in Fig. 4, which are different in two magnetic field orientations.

For the in-plane magnetic fields, $I_c(B)$ shows fast aperiodic fluctuations in Figs. 4a–4c. No distinct period could be detected at least for the field step as small as $\Delta B = 0.01$ mT. We check, that our procedure gives I_c values, which are perfectly stable at fixed magnetic field, as demonstrated in Fig. 5a. The maximum I_c deviation over 1000 curves is about 0.005 mA at $B = -1.4$ mT, which is negligible comparing to the observed fluctuations' amplitude 0.05 mA in Fig. 4c. Thus, the fluctuations are controlled by the external magnetic field, although they are found to be aperiodic.

On the contrary, no noticeable fluctuations can be observed for normal magnetic field orientation (see Figs. 4d–4f). The curves for the up (blue) and down (red) sweeps are reversed, but in addition there is an interplay between maximum and minimum in $I_c(B)$ at ± 12 mT, which is well known for the Josephson spin valves [30–34].

Temperature dependence of the critical current $I_c(T)$ is shown in Fig. 5b. It closely reminds the temperature dependencies observed in a half-metallic CrO_2 based long Josephson junctions [24].

4. DISCUSSION

As a result, we observe $I_c(B)$ pattern asymmetry and its' reversal in dependence on the magnetic field sweep direction. This effect can be observed for both

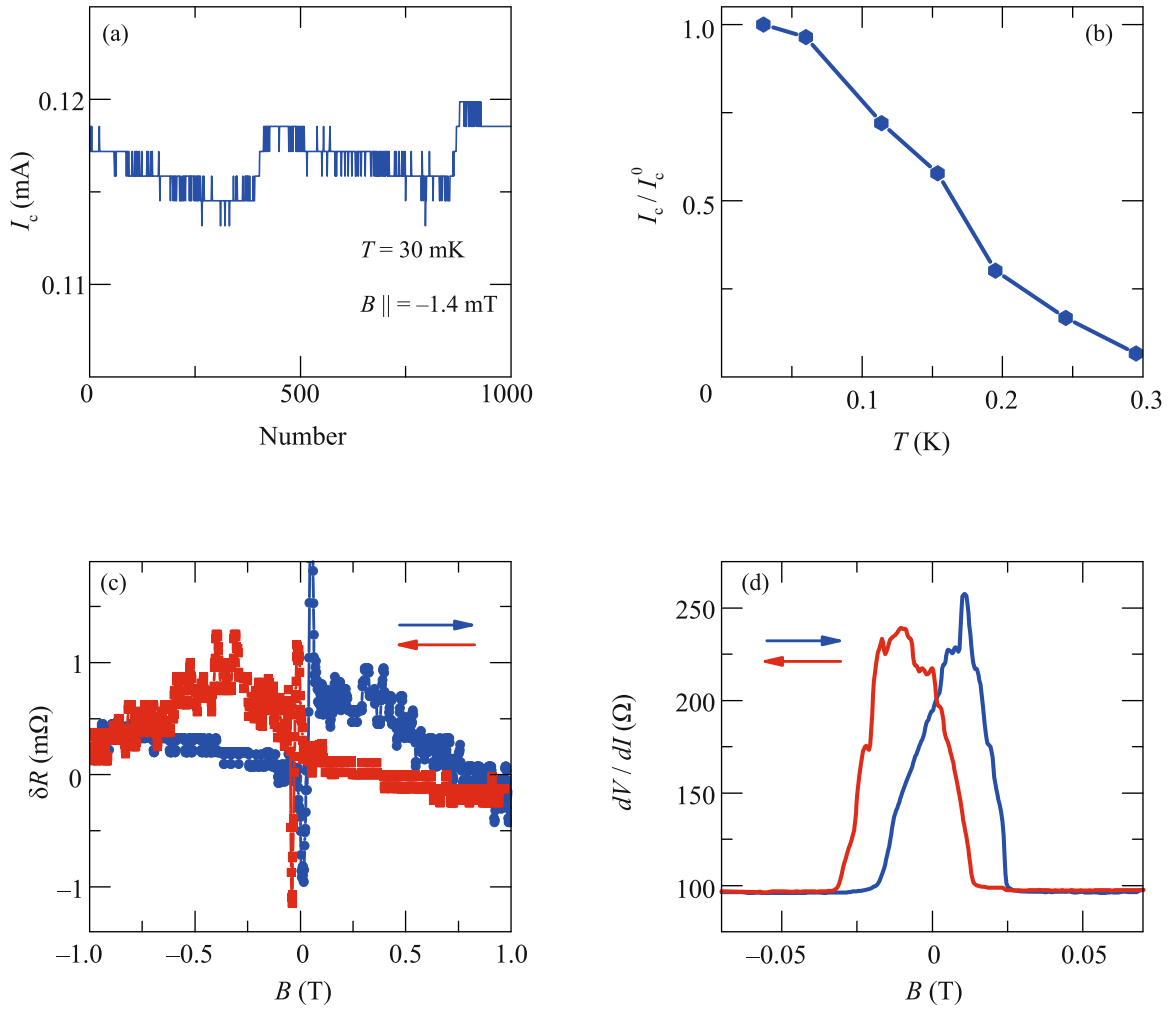

Fig. 5. (Color online) (a) Stability of I_c, as it is demonstrated for 1000 sequentially recorded curves at a fixed in-plane field value $B = -1.4$ mT. The maximum I_c deviation is about 0.005 mA at $B = -1.4$ mT, which is negligible comparing to the fluctuations' amplitude 0.05 mA in Fig. 4c. (b) Temperature dependence of I_c for S2 in zero field, which closely reminds the temperature dependencies observed in a half-metallic CrO_2 based long Josephson junctions [24]. (c) Typical spin-valve hysteresis [13, 14] in magnetoresistance of a single Au-FGT junction for the reference FGT flake. Blue and red curves correspond to the up and down magnetic field sweeps, respectively. In FGT, spin-polarized surface state acts as a source of spin, while spin-dependent scattering within the ferromagnet results in the resistance dependence on the magnetization direction. (d) Magnetic-field suppression of Andreev reflection for a single weakly-transparent In-FGT junction (the subgap resistance exceeds the normal value) in normal magnetic field at $T = 30$ mK. $dV/dI(B)$ curves are reversed for two sweep directions, similarly to the transparent In-FGT-In junctions.

magnetic field orientations, while in normal magnetic fields there is also a prominent change of the $I_c(B)$ shape during remagnetization.

This behavior cannot be expected for usual SFS junctions with the homogeneous magnetization of the central ferromagnetic layer, where remagnetization can only shift the $I_c(B)$ pattern position in magnetic field [24, 31]. On the other hand, the observed behavior is a known fingerprint of Josephson spin valves [30–34]. While in conventional Josephson junctions supercurrent is modulated by magnetic flux, in JSVs it is mainly defined by the relative orientation of magnetic layers, giving rise to the $I_c(B)$ asymmetry and reversal.

A conventional spin valve, in its simplest form, is a layered structure consisting of a thick (fixed) and a thin (free) ferromagnetic layers [13, 14]. Spin valve resistance is defined by the relative angle between magnetizations of the layers due to the spin-dependent scattering, which can be tuned by field or flowing current. Spin valve can be naturally realized in different types of topological materials and their heterostructures with ferromagnets [15–18]. In this case, spin-polarized topological surface state acts as one layer of a spin valve, while the role of the other is

played by the ferromagnetic lead or by the ferromagnetic sample's bulk [15, 17]. The spin-polarized surface state acts as a source of spin, while spin-dependent scattering within the ferromagnet results in a different resistance depending on the magnetization direction [15–18].

In the case of FGT, the presence of spin-polarized topological Fermi arcs has been demonstrated by ARPES [8], while spin momentum locking [56] was inferred to be responsible for anti-symmetric magnetoresistance in FGT/graphite/FGT heterostructures [12]. Thus, a FGT flake may be regarded as a spin valve, this scenario is independently verified by magnetoresistance of a single Au-FGT junction for the reference Hall bar sample in Fig. 5c, where typical spin-valve hysteresis is observed [13, 14]. Moreover, Fig. 4 shows asymmetric resistive features even at high currents, i.e., for the suppressed superconductivity (for 2–10 Ω junction resistance). These features are also reversed for two magnetic field directions, which confirms spin-valve behavior in FGT.

If a spin valve is sandwiched between two superconducting electrodes [30–34] (see Fig. 6), asymmetric $I_c(B)$ pattern should be reversed after remagnetization. For the magnetic topological materials it naturally implies spin triplet superconductivity. Effectiveness of singlet–triplet conversion depends on magnetic orientation misalignment, so $I_c(B)$ pattern depends on the spin-valve configuration. Due to the hysteresis in magnetization of a spin valve [13, 14], $I_c(B)$ demonstrates a mirror reversal in the opposite field sweeps [30, 31].

The observed interplay between the $I_c(B)$ maximum and minimum after remagnetization in Figs. 4d–4f is very unusual. Generally, this behavior requires breaking of certain symmetries. For FGT, the inversion symmetry breaking is known at the interface [36]. This is supported by a number of experimental observations of the skyrmion-like spin textures, e.g., Bloch-type [57] and Nol-type [36, 58, 59] skyrmions, domain wall twists [60], and chiral spin textures [61, 62]. Inversion symmetry breaking in a system with a large spin–orbit interactions gives rise to the spin–orbit torque, comprising terms which are even and odd in magnetization. The relative signs of the terms changes under remagnetization, violating the reversal of the $I_c(B)$ pattern in Figs. 4d–4f. This interplay in $I_c(B)$ is not observed in Figs. 4a–4c, since the FGT magnetization is not collinear to the out-of-plane current-induced polarization in this case. We wish to note, that one cannot ascribe the observed interplay to the spin valve memory effect [30, 32], since every remagnetization process starts from the same $B = \pm 100$ mT in our experiment.

Similar behavior can be reported for a single weakly-transparent In-FGT Andreev junction (the subgap resistance exceeds the normal one value) in Fig. 5d. $dV/dI(B)$ curves are reversed for two sweep directions, similarly to the highly-transparent In-FGT-In junctions in Fig. 3, so the spin-valve effect does not appear from disorder [63] in our samples.

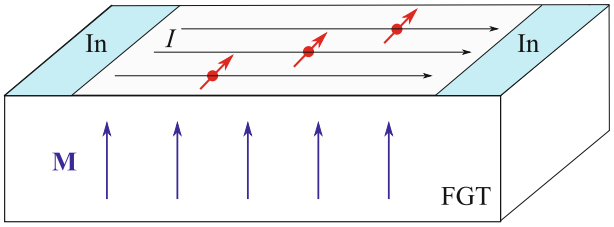

Fig. 6. (Color online) Sketch of the Josephson spin valve, which is realized in In-FGT-In junctions due to the spin-polarized surface state in the magnetic nodal-line topological semimetal FGT. Supercurrent (partially) flows through the spin polarized surface state (grey region) with complicated spin polarization, while spin-dependent scattering with the magnetized FGT bulk is responsible for the spin valve behavior.

Regarding the effects of the domain structure, one should note that the presence of several ferromagnetic domains between the superconducting leads could generally give rise to essentially the same physics as in a JSV [64, 65]. In particular, asymmetric non-Fraunhofer $I_c(B)$ patterns in SFS junctions with a complex multidomain structure have been reported before [54, 55]. However, the domain structure effects are hardly responsible for the results obtained in this paper. Sufficiently thick FGT samples within the low-temperature range $\lesssim 5$ K contain several types of domains [66, 67], among which bubble-like domains with comparatively small sizes, about a few hundred nanometers, are randomly distributed over the surface, introducing a substantial stochastic component to the domain structure [67]. We would like to emphasize here, that the asymmetric $dV/dI(B)$ curves and $dV/dI(B, I)$ colormaps in Figs. 3, 4 are highly reproducible, and therefore should not be attributed to any stochastic interfacial domain structures that would prevent to reproduce the results with an observed accuracy. Although, the non-coplanar spin textures [10] could noticeably contribute to aperiodic variations presented in Figs. 4a–4c for the in-plane field orientation, similarly to stochastic variations of $I_c(B)$ in [54, 55] for SFS junctions with multi domain barriers.

Thus, our experimental results can be regarded as demonstration of the JSV, which is realized in the magnetic nodal-line topological semimetal FGT. Moreover, surface transport was ubiquitously attributed to carry Josephson current at long distances in JJs based on topological materials [19–23], which supports the overall interpretation.

ACKNOWLEDGMENTS

We are grateful to V.T. Dolgopolov, A.S. Melnikov, and V.V. Ryazanov for fruitful discussions, and S.S. Khasanov for X-ray sample characterization.

FUNDING

This work was supported by the Russian Science Foundation, project no. 22-22-00229, https://rscf.ru/project/22-22-00229/.

CONFLICT OF INTEREST

The authors declare that they have no conflicts of interest.

REFERENCES

1. Y. Deng, Y. Yu, Y. Song, J. Zhang, N. Z. Wang, Z. Sun, Y. Yi, Y. Z. Wu, S. Wu, J. Zhu, J. Wang, X. H. Chen, and Y. Zhang, Nature (London, U.K.) **563**, 94 (2018). https://doi.org/10.1038/s41586-018-0626-9
2. J.-J. Guo, Q.-L. Xia, X.-G. Wang, Y.-Z. Nie, R. Xiong, and G.-H. Guo, J. Magn. Magn. Mater. **527**, 167719 (2021). https://doi.org/10.1016/j.jmmm.2020.167719
3. C. Tan, J. Lee, S. G. Jung, T. Park, S. Albarakati, J. Partridge, M. R. Field, D. G. McCulloch, L. Wang, and C. Lee, Nat. Commun. **9**, 1554 (2018). https://doi.org/10.1038/s41467-018-04018-w
4. H. L. Zhuang, P. R. C. Kent, and R. G. Henning, Phys. Rev. B **93**, 134407 (2016).
5. L. Cai, C. Yu, L. Liu, W. Xia, H.-A. Zhou, L. Zhao, Y. Dong, T. Xu, Z. Wang, Y. Guo, Y. Zhao, J. Zhang, L. Yang, L. Yang, and W. Jiang, Appl. Phys. Lett. **117**, 192401 (2020). https://doi.org/10.1063/5.0030607
6. B. Chen, J. H. Yang, H. D. Wang, M. Imai, H. Ohta, C. Michioka, K. Yoshimura, and M. H. Fang, J. Phys. Soc. Jpn. **82**, 124711 (2013).
7. Y. Wang, C. Xian, J. Wang, B. Liu, L. Ling, L. Zhang, L. Cao, Z. Qu, and Y. Xiong, Phys. Rev. B **96**, 134428 (2017).
8. K. Kim, J. Seo, E. Lee, K.-T. Ko, B. S. Kim, Bo G. Jang, J. M. Ok, J. Lee, Y. J. Jo, W. Kang, J. H. Shim, C. Kim, H. W. Yeom, B. I. Min, B.-J. Yang, and J. S. Kim, Nat. Mater. **17**, 794 (2018).
9. J. Xu, W. A. Phelan, and C.-L. Chien, Nano Lett. **19**, 8250 (2019).
10. Y. You, Y. Gong, H. Li, Z. Li, M. Zhu, J. Tang, E. Liu, Y. Yao, G. Xu, F. Xu, and W. Wang, Phys. Rev. B **100**, 134441 (2019).
11. Y. Zhang, H. Lu, X. Zhu, S. Tan, W. Feng, Q. Liu, W. Zhang, Q. Chen, Y. Liu, X. Luo, D. Xie, L. Luo, Z. Zhang, and X. Lai, Sci. Adv. **4**, eaao6791 (2018). https://doi.org/10.1126/sciadv.aao6791
12. S. Albarakati, C. Tan, Z. Chen, J. G. Partridge, G. Zheng, L. Farrar, E. L. H. Mayes, M. R. Field, C. Lee, Y. Wang, Y. Xiong, M. Tian, F. Xiang, A. R. Hamilton, O. A. Tretiakov, D. Culcer, Y. Zhao, and Y. Wang, Sci. Adv. **5**, eaaw0409 (2019). https://doi.org/10.1126/sciadv.aaw0409
13. M. Tsoi, A. G. M. Jansen, J. Bass, W.-C. Chiang, M. Seck, V. Tsoi, and P. Wyder, Phys. Rev. Lett. **80**, 4281 (1998).
14. E. B. Myers, D. C. Ralph, J. A. Katine, R. N. Louie, and R. A. Buhrman, Science (Washington, DC, U. S.) **285**, 867 (1999).
15. V. D. Esin, D. N. Borisenko, A. V. Timonina, N. N. Kolesnikov, and E. V. Deviatov, Phys. Rev. B **101**, 155309 (2020).
16. A. Kononov, O. O. Shvetsov, A. V. Timonina, N. N. Kolesnikov, and E. V. Deviatov, JETP Lett. **109**, 180 (2019).
17. O. O. Shvetsov, V. D. Esin, A. V. Timonina, N. N. Kolesnikov, and E. V. Deviatov, Europhys. Lett. **127**, 57002 (2019).
18. J. Tian, I. Miotkowski, S. Hong, and Y. P. Chen, Sci. Rep. **5**, 14293 (2015).
19. J. H. Lee, G.-H. Lee, J. Park, J. Lee, S.-G. Nam, Y.-S. Shin, J. S. Kim, and H.-J. Lee, Nano Lett. **14**, 5029 (2014).
20. A. Kononov, O. O. Shvetsov, S. V. Egorov, A. V. Timonina, N. N. Kolesnikov, and E. V. Deviatov, Europhys. Lett. **122**, 27004 (2018).
21. C. Huang, B. T. Zhou, H. Zhang, B. Yang, R. Liu, H. Wang, Y. Wan, K. Huang, Z. Liao, E. Zhang, S. Liu, Q. Deng, Y. Chen, X. Han, J. Zou, X. Lin, Z. Han, Y. Wang, K. Tuen Law, and F. Xiu, Nat. Commun. **10**, 2217 (2019).
22. O. O. Shvetsov, V. D. Esin, Yu. S. Barash, A. V. Timonina, N. N. Kolesnikov, and E. V. Deviatov, Phys. Rev. B **101**, 035304 (2020).
23. Y. Wang, S. Yang, P. K. Sivakumar, B. R. Ortiz, S. M. L. Teicher, H. Wu, A. K. Srivastava, C. Garg, D. Liu, S. S. P. Parkin, E. S. Toberer, T. McQueen, S. D. Wilson, and M. N. Ali, arXiv: 2012.05898.
24. R. S. Keizer, S. T. B. Goennenwein, T. M. Klapwijk, G. Miao, G. Xiao, and A. Gupta, Nature (London, U.K.) **439**, 825 (2006).
25. F. S. Bergeret, A. F. Volkov, and K. B. Efetov, Phys. Rev. Lett. **86**, 4096 (2001).
26. F. S. Bergeret, A. F. Volkov, and K. B. Efetov, Rev. Mod. Phys. **77**, 1321 (2005).

27. P. Dutta, F. Parhizgar, and A. M. Black-Schaffer, Phys. Rev. B **101**, 064514 (2020).

28. F. S. Bergeret and I. V. Tokatly, Phys. Rev. Lett. **110**, 117003 (2013).

29. F. S. Bergeret and I. V. Tokatly, Phys. Rev. B **89**, 134517 (2014).

30. O. M. Kapran, A. Iovan, T. Golod, and V. M. Krasnov, Phys. Rev. Res. **2**, 013167 (2020).

31. N. Banerjee, J. W. A. Robinson, and M. G. Blamire, Nat. Commun. **5**, 4771 (2014).

32. B. M. Niedzielski, T. J. Bertus, J. A. Glick, R. Loloee, W. P. Pratt, Jr., and N. O. Birge, Phys. Rev. B **97**, 024517 (2018).

33. N. Satchell, P. M. Shepley, M. Algarni, M. Vaughan, E. Darwin, M. Ali, M. C. Rosamond, L. Chen, E. H. Linfield, B. J. Hickey, and G. Burnell, Appl. Phys. Lett. **116**, 022601 (2020).

34. E. C. Gingrich, B. M. Niedzielski, J. A. Glick, Y. Wang, D. L. Miller, R. Loloee, W. P. Pratt, Jr., and N. O. Birge, Nat. Phys. **12**, 564 (2016).

35. T. Yu. Karminskaya, M. Yu. Kupriyanov, and A. A. Golubov, JETP Lett. **87**, 570 (2008).

36. T.-E. Park, L. Peng, J. Liang, et al., Phys. Rev. B **103**, 104410 (2021).

37. K. Garello, I. M. Miron, C. O. Avci, F. Freimuth, Y. Mokrousov, S. Blügel, S. Auffret, O. Boulle, G. Gaudin, and P. Gambardella, Nat. Nanotechnol. **8**, 587 (2013).

38. X. Qiu, Z. Shi, W. Fan, S. Zhou, and H. Yang, Adv. Mater. **30**, 1705699 (2018).

39. A. Manchon, J. Železný, I. M. Miron, T. Jungwirth, J. Sinova, A. Thiaville, K. Garello, and P. Gambardella, Rev. Mod. Phys. **91**, 035004 (2019).

40. H. Kurebayashi, J. Sinova, D. Fang, A. C. Irvine, T. D. Skinner, J. Wunderlich, V. Novák, R. P. Campion, B. L. Gallagher, E. K. Vehstedt, L. P. Zârbo, K. Výborný, A. J. Ferguson, and T. Jungwirth, Nat. Nanotechol. **9**, 211 (2014).

41. Y.-T. Liu, C.-C. Huang, K.-H. Chen, Y.-H. Huang, C.-C. Tsai, T.-Y. Chang, and C.-F. Pai, arXiv: 2108.01272 (2021).

42. C.-Z. Chen, J. J. He, M. N. Ali, G.-H. Lee, K. C. Fong, and K. T. Law, Phys. Rev. B **98**, 075430 (2018).

43. N. F. Q. Yuan and L. Fu, arXiv: 2106.01909.

44. A. Buzdin, Phys. Rev. Lett. **101**, 107005 (2008).

45. F. Konschelle and A. Buzdin, Phys. Rev. Lett. **102**, 017001 (2009); Phys. Rev. Lett. **123**, 169901(E) (2019).

46. I. Kulagina and J. Linder, Phys. Rev. B **90**, 054504 (2014).

47. M. A. Silaev, I. V. Tokatly, and F. S. Bergeret, Phys. Rev. B **95**, 184508 (2017).

48. Yu. M. Shukrinov, I. R. Rahmonov, K. Sengupta, and A. Buzdin, Appl. Phys. Lett. **110**, 182407 (2017).

49. H.-J. Deiseroth, K. Aleksandrov, C. Reiner, L. Kienle, and R. K. Kremer, Eur. J. Inorg. Chem. **2006**, 1561 (2006).

50. N. P. Armitage, E. J. Mele, and A. Vishwanath, Rev. Mod. Phys. **90**, 015001 (2018).

51. O. O. Shvetsov, V. D. Esin, Yu. S. Barash, A. V. Timonina, N. N. Kolesnikov, and E. V. Deviatov, Phys. Rev. B **101**, 035304 (2020).

52. O. O. Shvetsov, V. D. Esin, A. V. Timonina, N. N. Kolesnikov, and E. V. Deviatov, Phys. Rev. B **99**, 125305 (2019).

53. O. O. Shvetsov, A. Kononov, A. V. Timonina, N. N. Kolesnikov, and E. V. Deviatov, JETP Lett. **107**, 774 (2018).

54. T. S. Khaire, W. P. Pratt, Jr., and N. O. Birge, Phys. Rev. B **79**, 094523 (2009).

55. M. A. Khasawneh, T. S. Khaire, C. Klose, W. P. Pratt, Jr., and N. O. Birge, Supercond. Sci. Technol. **24**, 024005 (2011).

56. S.-Y. Xu, C. Liu, S. K. Kushwaha, R. Sankar, J. W. Krizan, I. Belopolski, M. Neupane, G. Bian, N. Alidoust, T.-R. Chang, H.-T. Jeng, C.-Y. Huang, W.-F. Tsai, H. Lin, P. P. Shibayev, F.-C. Chou, R. J. Cava, and M. Z. Hasan, Science (Washington, DC, U. S.) **347**, 294 (2015).

57. B. Ding, Z. Li, G. Xu, H. Li, Z. Hou, E. Liu, X. Xi, F. Xu, Y. Yao, and W. Wang, Nano Lett. **20**, 868 (2020).

58. Y. Wu, S. Zhang, J. Zhang, W. Wang, Y. L. Zhu, J. Hu, G. Yin, K. Wong, C. Fang, C. Wan, X. Han, Q. Shao, T. Taniguchi, K. Watanabe, J. Zang, Z. Mao, X. Zhang, and K. L. Wang, Nat. Commun. **11**, 3860 (2020).

59. M. Yang, Q. Li, R. V. Chopdekar, R. Dhall, J. Turner, J. D. Carlström, C. Ophus, C. Klewe, P. Shafer, A. T. N'Diaye, J. W. Choi, G. Chen, Y. Z. Wu, C. Hwang, F. Wang, and Z. Q. Qiu, Sci. Adv. **6**, eabb5157 (2020).

60. L. Peng, F. S. Yasin, T.-E. Park, S. J. Kim, X. Zhang, T. Nagai, K. Kimoto, S. Woo, and X. Yu, arxiv: 2105.00468.
https://doi.org/10.1002/adfm.202103583

61. H.Wang, C.Wang, Y. Zhu, Z.-A. Li, H. Zhang, H. Tian, Y. Shi, H. Yang, and J. Li, arxiv: 1907.08382.

62. M. J. Meijer, J. Lucassen, R. A. Duine, H. J. M. Swagten, B. Koopmans, R. Lavrijsen, and M. H. D. Guimarães, Nano Lett. **20**, 8563 (2020).

63. S. Singh, R. Rawat, S. Esakki Muthu, et al., Phys. Rev. Lett. **109**, 246601 (2012).

64. A. Konstandin, J. Kopu, and M. Eschrig, Phys. Rev. B **72**, 140501(R) (2005).

65. E. Bhatia, A. Srivastava, J. Devine-Stoneman, N. A. Stelmashenko, Z. H. Barber, J. W. A. Robinson, and K. Senapati, Nano Lett. **21**, 3092 (2021).

66. N. León-Brito, E. D. Bauer, F. Ronning, J. D. Thompson, and R. Movshovich, J. Appl. Phys. **120**, 083903 (2016).

67. G. D. Nguyen, J. Lee, T. Berlijn, Q. Zou, S. M. Hus, J. Park, Z. Gai, C. Lee, and A.-P. Li, Phys. Rev. B **97**, 014425 (2018).